Materials Advances

ROYAL SOCIETY OF CHEMISTRY

PAPER

View Article Online
View Journal | View Issue

Cite this: *Mater. Adv.*, 2024, 5, 8223

Rational design of single-atom catalysts for efficient H_2O_2 production *via* a four-step strategy†

Shu-Long Li,[abc] Xiaogui Song,[a] Zuhui Zhou,[a] Hongyuan Zhou,[a] Liang Qiao,*[b] Yong Zhao*[ad] and Li-Yong Gan*[e]

Received 19th July 2024,
Accepted 16th September 2024

DOI: 10.1039/d4ma00732h

rsc.li/materials-advances

Electrocatalysis presents an efficient and eco-friendly approach for the two-electron oxygen reduction reaction ($2e^-$ ORR) to produce hydrogen peroxide (H_2O_2). However, challenges persist in enhancing catalyst activity and refining design strategies. In this study, a general four-step strategy is introduced to develop efficient single-atom catalysts (SACs) for H_2O_2 production based on transition metals and nonmetals embedded into γ-graphyne monolayers (TM–NM–GY) through first-principles calculations. Our results indicate that the intrinsic activity for the $2e^-$ ORR can be properly and handily evaluated using the robust intrinsic electronegativity descriptor. On this foundation, we propose two strategies of B doping and creating C vacancies (v) to further enhance catalytic activity. Remarkably, Ni–B–GY and Ag–v–GY exhibit exceptional selectivity, stability, and activity with overpotentials as low as 0.08 V and 0.15 V, respectively, approaching the ideal limit of H_2O_2 catalysts. Mechanistic investigations reveal that B doping facilitates electron transfer and strengthens the hybridization between Ni 3d and O 2p orbitals, leading to stronger adsorption strength of *OOH and thus enhancing the $2e^-$ ORR catalytic performance. These findings not only present several promising SAC candidates for H_2O_2 production, but also pave the way for the rational design of highly efficient SACs for various catalytic reactions.

1. Introduction

Hydrogen peroxide (H_2O_2) is a versatile industrial chemical used in various applications such as medical treatment, bleaching, disinfection, chemical synthesis, wastewater treatment, and energy production.[1–3] A conventional method for producing H_2O_2, known as the anthraquinone process, is complex and energy-intensive, and in particular, generates toxic by-products, and thus poses severe safety risks.[4,5] In contrast, electrochemical synthesis offers a more sustainable and energy-efficient approach, drawing significant interest from the community. This process involves the two-electron ($2e^-$) oxygen reduction reaction (ORR), where oxygen (O_2) is directly converted to H_2O_2 ($O_2 + 2H^+ + 2e^- \rightarrow H_2O_2$).[6,7] While noble metals like Pd or Au have been employed as catalysts for H_2O_2 production, their scarcity and high cost limit their widespread commercial application.[8–10] Challenges include the selectivity for the $2e^-$ ORR pathway to H_2O_2 competing with the four-electron ($4e^-$) ORR pathway to H_2O, as well as the poor stability of most catalysts at thermodynamic synthesis potentials.[2] Therefore, it is crucial to develop efficient electrocatalysts with high stability, activity, selectivity, and atomic utilization rate for H_2O_2 production.

Transition metal (TM) single-atom catalysts (SACs) are emerging as promising catalysts due to their nearly 100% utilization of active metals, high activity, durability, low coordination environment, and strong interaction with supports.[11–14] These benefits have enabled the successful use of SACs in various reactions such as the ORR,[15–21] oxygen evolution reaction (OER),[22,23] nitrogen reduction reaction (NRR)[24–29] and carbon dioxide reduction reaction (CO_2RR).[30,31] Currently, the application of TM-SAC in H_2O_2 production is still in its infancy, and its potential has not yet been fully demonstrated. Creating a complete picture that not only reveals trends and origin of activity, but also facilitates the development of efficient catalysts is critical for H_2O_2 production. However, major efforts have mainly centered on understanding the trends and origins of activity, rendering the design still far from satisfactory.

---

[a] Institute for Advanced Study, Chengdu University, Chengdu 610106, China. E-mail: zhaoyong@cdu.edu.cn
[b] School of Physics, University of Electronic Science and Technology of China, Chengdu 611700, China. E-mail: liang.qiao@uestc.edu.cn
[c] Western Superconducting Technologies Co, Ltd., Xi'an 710018, China
[d] College of Physics and Energy, Fujian Normal University, Fuzhou 350117, China
[e] College of Physics and Center of Quantum Materials and Devices, Chongqing University, Chongqing 401331, China. E-mail: ganly@cqu.edu.cn

† Electronic supplementary information (ESI) available. See DOI: https://doi.org/10.1039/d4ma00732h

In recent years, numerous two-dimensional (2D) materials, including graphene,[32] g-C_3N_4,[33] C_2N,[34] MoS_2,[35] porphyrin,[36] and phthalocyanine,[37] have been reported as carriers for SACs. However, the selection of all-carbon materials as carriers for SACs presents significant challenges. The drift of graphene and MoS_2, along with the weak interaction between transition metal (TM) and carbon (C), hinders the effective dispersion of TM atoms. To address this limitation, researchers must employ various complex and precise methods, such as constructing defects,[29] applying strain,[18] or forming TM–N_x complexes.[20] Additionally, the high cost and limited solubility of porphyrin and phthalocyanine organic molecules restrict their application under specific solvents or reaction conditions.[38] In contrast, exploring all-carbon materials with uniformly porous structures that can securely anchor active TM atoms in their pore positions may present a promising approach for SACs.

Graphyne (GY) is a newly discovered 2D porous material, similar to g-C_3N_4 and C_2N, which has garnered significant attention following its successful synthesis.[39–41] Composed of sp^2 and sp hybridized C units (–C=C– and –C≡C–), GY exhibits advantageous properties, including enhanced conjugation, porosity and stability.[42–44] These significant characteristics of GY endow TM-anchored GY (TM–GY) with strong structural stability and demonstrate excellent catalytic potential in the ORR and NRR.[25,45] However, the exploration of TM–GY, as well as TM and non-metal (NM) co-doped GY (TM–NM–GY), as potential SACs for H_2O_2 production is still in its early stages.[46] Several unresolved issues remain: (i) Is there a universal strategy to assess outstanding SACs for H_2O_2 production? (ii) Are there intrinsic descriptors that effectively characterize activity trends and origins? (iii) Are there some effective strategies for further optimizing activity?

In this study, first-principles calculations were used to comprehensively assess the potential of $2e^-$ ORR electrocatalysts among 30 types of TM–GY and 15 types of TM–NM–GY SACs *via* a general four-step strategy: (i) evaluating catalytic activity and designing intrinsic activity descriptors; (ii) enhancing activity through NM doping; (iii) assessing the selectivity; and (iv) examining the stability (Fig. 1(a)). Ag–, Cu–, Ni–, Pd–, and Pt–GY were identified as efficient SACs toward the $2e^-$ ORR with outstanding catalytic activity. Two reliable intrinsic activity descriptors φ_1 and φ_2 were established for the screening and designing of $2e^-$ ORR catalysts. Based on the descriptors, B doping and creating C vacancies were shown to be effective strategies for further enhancing catalytic activity, with Ni–B–GY and Ag–v–GY demonstrating outstanding activity. Particularly, Ni–B–GY exhibited superior activity, selectivity, and stability with a significantly lower overpotential of 0.08 V. The four-step screening strategy and descriptors introduced in this study are anticipated to offer insights and guidance for the design and prediction of other catalysts.

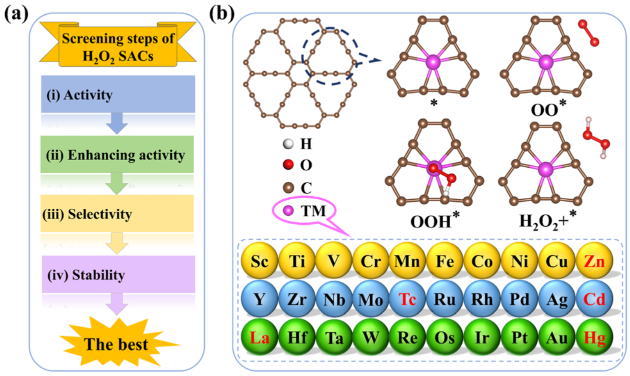

Fig. 1 (a) Schematic diagram of screening H_2O_2 SACs. (b) $2e^-$ ORR pathways on TM–GY.

2. Computational details

All spin-polarized density functional theory (DFT) calculations were performed using the Vienna ab initio simulation package.[47] The electron-ion interactions were described using the projector augmented-wave-method.[48] For accurate electron exchange–correlation, the Perdew–Burke–Ernzerhof functional within the generalized gradient approximation framework was employed.[49] Additionally, the DFT+D2 method was applied to correct for van der Waals forces between the adsorbent carrier and the adsorbate.[50] The lattice parameter of GY was 6.89 Å. A 2 × 2 × 1 GY supercell was employed to simulate electrocatalysis for H_2O_2 production, as the distance of 6.89 Å between the TM atoms is adequate for accurately evaluating the interactions between the TM and the adsorbates. A vacuum thickness of 15 Å was introduced to avoid preventing periodic interactions. The plane wave cut-off energy was set at 500 eV. The residual forces and energy convergence criteria were maintained below 0.02 eV $Å^{-1}$ and 10^{-5} eV, respectively. Structural relaxation and electronic structure analyses were performed using 3 × 3 × 1 and 7 × 7 × 1 Γ-centered k-points to sample the Brillouin zone, respectively. The crystal orbital Hamilton population (COHP) method was used to explore the interaction between the active center and the intermediates.[51,52] The thermodynamic stability of the catalyst was assessed through *ab initio* molecular dynamics (AIMD) simulations and the radial distribution function (RDF) analysis at 300 K.

The binding energy (E_{bind}), adsorption energy (ΔE), Gibbs free energy (ΔG) of intermediates, limiting potential (U_L) and the overpotential (η) were calculated using the following equations:

$$E_{\text{bind}} = E_{\text{TM-GY}} - E_{\text{GY}} - E_{\text{TM}} \quad (1)$$

$$\Delta E = E_{\text{ads-TM-GY}} - E_{\text{TM-GY}} - E_{\text{ads}} \quad (2)$$

$$\Delta G = \Delta E + \Delta \text{ZPE} - T\Delta S + \Delta G_{\text{U}} \quad (3)$$

$$U_{\text{L}} = \max \Delta G/e \quad (4)$$

$$\eta = U_{\text{L}} - U_{\text{eq}} \quad (5)$$

where $E_{\text{TM-GY}}$ and E_{GY} represent the total energy of GY with and without bound TM, E_{TM} is the energy of an isolated TM atom. $E_{\text{ads-TM-GY}}$ and E_{ads} represent the total energy of the catalyst with the adsorbed adsorbate and the free adsorbate. ΔZPE and

ΔS indicate changes in zero-point energy and entropy; T represents room temperature at 298.15 K. The ΔG_U is the free energy change under an applied voltage, $\Delta G_U = -neU$, where n is the number of transferred electrons. U_L is the potential of the potential determining step (PDS). The equilibrium potential (U_{eq}) is 0.7 V.[53] More details can be found in the ESI.†

3. Results and discussion

The sp^2 and sp^3 hybridized C sites in GY lack the ability to adsorb O_2 due to their limited positive charge or the absence of empty orbitals for accepting lone pair electrons from O_2 (Fig. S1, ESI†). Conversely, the sp hybridized C site (–C≡C–) demonstrates strong O_2 adsorption capacity, resulting in the dissociation of the OOH* intermediate into O* + OH* (* represents the catalyst), ultimately hindering the generation of H_2O_2. Thus, pure GY is ineffective for H_2O_2 production. Our focus then shifted towards developing TM–GY as a highly active H_2O_2 SACs. Previous studies have demonstrated TM atoms can be effectively incorporated into GY cavities due to the reactivity of sp-hybridized –C≡C– bonds.[54] Therefore, TM was directly bound to a 2 × 2 × 1 GY supercell for 2e⁻ ORR in this study.

To efficiently identify whether SACs are suitable for electrochemical H_2O_2 synthesis with high activity, stability, and selectivity, we established a general four-step strategy (Fig. 1(a)): (a) evaluating the catalytic activity and designing intrinsic activity descriptors of TM–GY SACs for H_2O_2 production; (b) enhancing the catalytic activity of TM–GY SACs through NM doping (TM–NM–GY) based on intrinsic activity descriptors; (c) assessing the selectivity of TM–GY and TM–NM–GY; (d) examining the stability of TM–GY and TM–NM–GY.

3.1 Screening efficient catalytic activity of TM–GY SACs for H_2O_2

Thirty types of TM–GY (TM = 3d–5d) were studied to screen efficient SACs for H_2O_2 production, as shown in Fig. 1(b). After excluding radioactive or toxic elements (Tc, Cd, and Hg), lanthanides (La), and metals that cannot bind to GY (Zn),[54] only 25 types of TM–GY remained on the screening list.

The adsorption of O_2 molecules on TM–GY is a crucial prerequisite for the 2e⁻ ORR to generate H_2O_2. Failure to adsorb O_2 would hinder the subsequent hydrogenation reaction to produce H_2O_2. Therefore, both side-on and end-on adsorption configurations of O_2 on all TM–GY catalysts were examined. Results indicate that O_2 cannot be adsorbed on Au–GY due to its positive Gibbs free energy change (ΔG_{OO}) of 0.24 eV, leading to the exclusion of Au–GY from further screening. Among the other TM–GY catalysts, O_2 is adsorbed predominantly in the side-on configuration, except on Cu–, Ni– and Ag–GY, as shown in Fig. S2 (ESI†). Following successful O_2 adsorption, the 2e⁻ ORR progresses to a hydrogenation step, forming the OOH* intermediate without breaking the O–O bond. A linear relationship between ΔG_{OOH} and ΔG_{OO}, is observed with a coefficient of 0.81 (Fig. S3, ESI†), indicating that the ΔG_{OO} and the catalytic activity of H_2O_2 can be represented by a single intermediate free energy descriptor of ΔG_{OOH}.

The overpotential (η) is a critical parameter to assess the catalytic activity for H_2O_2 production. An effective

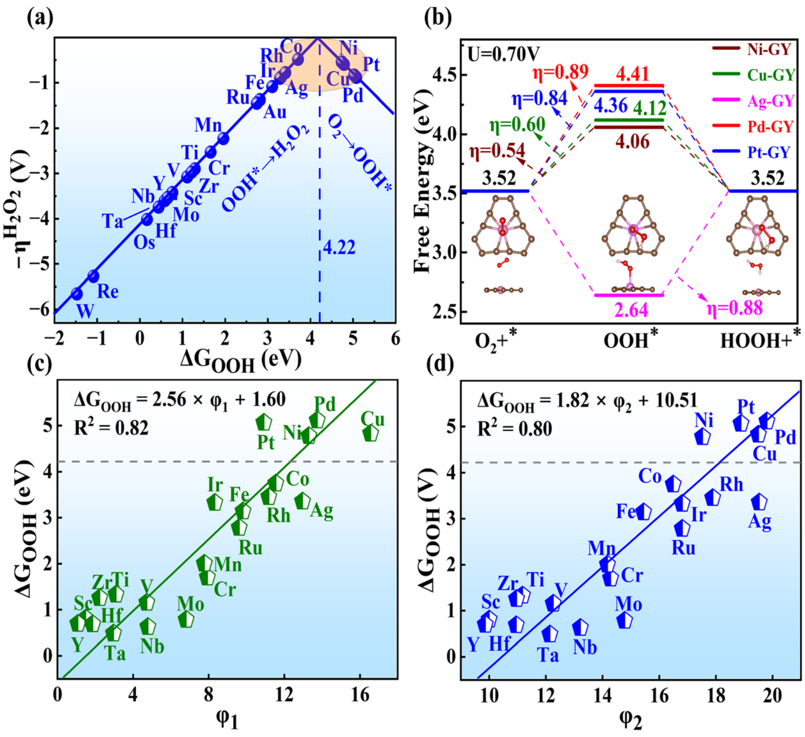

Fig. 2 (a) The volcano plot of ΔG_{OOH} and the overpotential. (b) Free energy diagram for 2e⁻ ORR on TM–GY candidates (TM = Ni, Cu, Ag, Pd and Pt). (c) and (d) The scaling relationship between ΔG_{OOH} and φ_1, φ_2 for TM–GY.

electrocatalyst should have an ideal η close to 0 V ($U_L = U_{eq} = 0.7$ V).[40] Subsequently, the η on all TM–GY was determined using the standard hydrogen electrode method.[55] As shown in Fig. 2(a), the activity trend picture illustrated a linear relationship resembling a volcano plot between ΔG_{OOH} and η of TM–GY. A closer alignment of ΔG_{OOH} and η values towards the peak of the volcano plot, indicates superior catalytic performance. Particularly, the significantly negative ΔG_{OOH} values at the bottom of the left leg suggest strong interactions between OOH and TM–GY. Following the Sabatier principle,[56] excessively strong intermediates may hinder the formation and release of the H_2O_2 product, leading to the potential determining step (PDS) occurring in the final step of ($OOH^* \rightarrow H_2O_2$). Conversely, weak ΔG_{OOH} values correspond to weak O_2 adsorption, which is unfavorable for subsequent hydrogenation steps, resulting in the PDS occurring in the initial step of ($O_2 \rightarrow OOH^*$). Upon evaluation, Ir–, Rh–, Ag–, Co–, Ni–, Cu–, Pd–, and Pt–GY exhibit moderate ΔG_{OOH} values close to 4.22 eV, indicating high catalytic activity. Additionally, we conducted a comparative study on the adsorption of OOH on GY, isolated Ni atom, and Ni–GY (Fig. S4, ESI†). The results indicate a synergistic interaction between GY and Ni atoms, which endows Ni–GY with an appropriate OOH adsorption strength, thereby facilitating the generation of H_2O_2. This may be the original cause of GY as a substrate for constructing SACs to produce H_2O_2.

It is noteworthy that the O–O bonds in the OOH* intermediates of Co–, Rh–, and Ir–GY underwent cleavage during the $OOH^* \rightarrow H_2O_2$ process, facilitating the formation of the O* intermediate and H_2O, as shown in Fig. S5 (ESI†). This suggests that they are unsuitable as SACs for H_2O_2 production. Conversely, Ni–, Cu–, Pd–, Ag–, and Pt–GY had stable O–O bonds in the OOH* intermediates, enabling the successful synthesis of H_2O_2. Following screening, only five TM–GY (TM = Ag, Cu, Ni, Pd, and Pt) were selected as potential candidates for further investigation.

To achieve a deeper comprehension of the reaction mechanisms, free energy diagrams for the $2e^-$ ORR process with U_L of 0.7 V were plotted in Fig. 2(b). The initial steps of $O_2 \rightarrow OOH^*$ for Ni–, Cu–, Pd– and Pt–GY exhibit slight uphill trends, indicating a requirement for a small energy input at this stage. Conversely, Ag–GY shows a thermodynamically downhill initial step, suggesting a spontaneous exothermic process. For the final step of $OOH^* \rightarrow H_2O_2$, all are spontaneous except for Ag–GY. The overall reaction pathway for H_2O_2 production reveals overpotentials of 0.54, 0.60, 0.89, 0.84 and 0.88 V for Ni–, Cu–, Pd–, Pt– and Ag–GY, respectively.

After confirming the catalytic activity of these TM–GY SACs, it is crucial to establish a reliable and simple intrinsic activity descriptor to gain deeper insights into the underlying activity trends and to facilitate the design of improvements for the most promising candidates. Given that electronegativity reflects the ability of atoms to attract electrons in chemical bonds, and considering that the number of d-electrons and atomic radius may influence adsorption performance, we summarized these factors in Table S1 (ESI†) and plotted their relationships with activity in the Fig. S6a–c (ESI†). The results indicate that d-electrons and electronegativity are negatively correlated with activity, while atomic radius shows a positive correlation with activity. In this study, we introduce two intrinsic electronegativity modified descriptors, φ_1 and φ_2 inspired by Zeng *et al.* for $4e^-$ ORR[57] and Ren *et al.* for CO_2 reduction,[58] as well as one electronic spin moment modified descriptor φ_3, inspired by Zhang *et al.* for NRR.[59] The calculations are as follows:

$$\varphi_1 = \alpha\theta_d \times \frac{E_{TM} + (n_C \times E_C)/(L-1)}{E_O} \tag{6}$$

$$\varphi_2 = (E_{TM} + n_C \times E_C) + \theta_d \tag{7}$$

$$\varphi_3 = \sqrt{\theta_d \times E_{TM}} \tag{8}$$

where α is the correction coefficient, θ_d and n_C represent the occupancy number in *d* orbitals and the coordination number of TM, respectively. L is the periodic number of the TM element in the periodic table (L = 4–6), and E_{TM}, E_C and E_O are the electronegativities of TM, C and O, respectively. Interestingly, three linear relationships are observed between ΔG_{OOH} and φ_1 (R^2 = 0.82) (Fig. 2(c)), ΔG_{OOH} and φ_2 (R^2 = 0.80) (Fig. 2(d)), ΔG_{OOH} and φ_3 (R^2 = 0.75) (Fig. S6d, ESI†). These findings clearly suggest that the ΔG_{OOH} and the activity of the $2e^-$ ORR can be more easily evaluated and predicted using intrinsic activity descriptor (φ_1, φ_2 or φ_3) rather than relying on complex DFT calculations. Specifically, a higher φ_1, φ_2 or φ_3 corresponds to a weaker ΔG_{OOH}. A weaker ΔG_{OOH} results in high catalytic activity when $\Delta G_{OOH} < 4.22$ eV, whereas a stronger ΔG_{OOH} results in high catalytic activity when $\Delta G_{OOH} > 4.22$ eV. Considering that the orbital occupancy and element electronegativity are inherent qualities and constants, thus, adjusting the coordination structure or coordination number may be the most convenient and effective way to regulate the values of φ_1, φ_2 or φ_3 for further activity enhancement.

3.2 Further enhancement of activity through NM modification

After identifying five TM–GY (TM = Ag, Cu, Ni, Pd, and Pt) as promising SAC candidates for $2e^-$ ORR to produce H_2O_2, it has been noted that there is significant space for improving their catalytic activity. By analyzing intrinsic activity descriptors, it is evident that the φ_1 or φ_2 values of these materials exceed the optimal activity point (intersection point φ_1 or φ_2 with 4.22), suggesting that reducing or adjusting the coordination number could be beneficial for enhancing the activity of these TM–GY. Previous studies have demonstrated that modification with NM such as B doping, N doping or creating C vacancies (v) can alter the coordination environment, thereby enhancing catalytic activity.[60–62] Therefore, TM–NM–GY (NM = B, N, and v) were used to enhance the $2e^-$ ORR activity, as shown in Fig. 3(a).

Our findings reveal that TM atoms serve as the active sites for capturing O_2 with a side-on configuration on Pt–NM–GY and Pd–NM–GY, while they tend to prefer an end-on configuration on other materials (Fig. S7, ESI†). After undergoing the NM modification, TM–NM–GY (TM = Cu, Ni, Pd, and Pt) demonstrates a significantly improved capacity for O_2 adsorption in comparison to TM–GY, as is evident from Fig. S8 (ESI†).

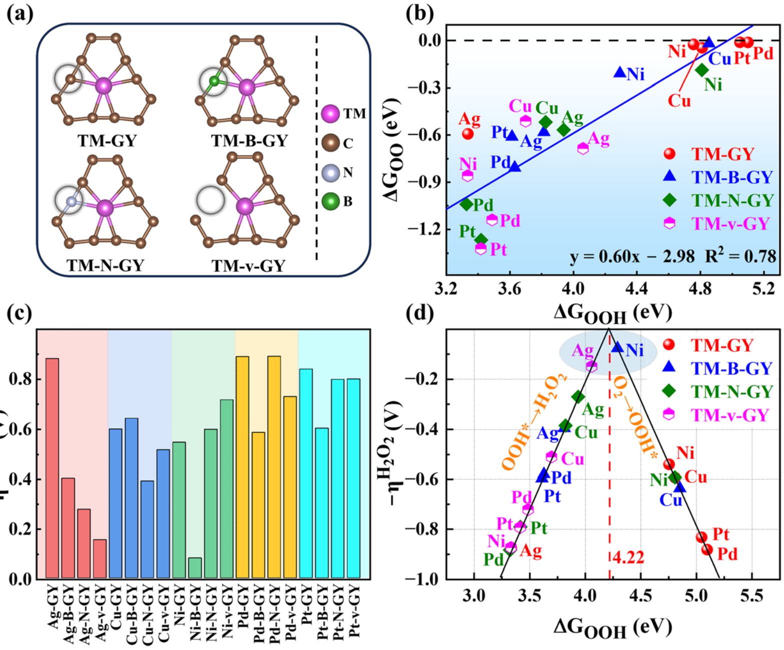

Fig. 3 (a) The configuration of TM–NM–GY (NM = B, N doping or C vacancy). (b) The linear relationship between ΔG_{OOH} and ΔG_{OO}. (c) The $\eta^{H_2O_2}$ for TM–NM–GY. (d) Volcano plot of ΔG_{OOH} as a function of overpotential $\eta^{H_2O_2}$.

Moreover, the C vacancy demonstrates a higher O_2 adsorption capacity than B or N doping. Furthermore, a linear correlation was observed between ΔG_{OO} and O–O bond length (Fig. S9, ESI†), indicating that stronger O_2 adsorption strength corresponds to longer O–O bonds. The negative ΔG_{OO} values and elongated O–O bonds indicate stable adsorption and activation of O_2, preparing for the subsequent hydrogenation reaction to produce H_2O_2. Subsequently, the hydrogenation step forming the OOH* intermediate was investigated (Fig. S7, ESI†). A strong linear relationship was also identified between ΔG_{OOH} and ΔG_{OO} with a coefficient of 0.78 (Fig. 3(b)), indicating that the H_2O_2 catalytic activity can be represented by a single descriptor of ΔG_{OOH}.

The catalytic activity of H_2O_2 on various TM–NM–GY catalysts was investigated through the analysis of free energy diagrams (Fig. S10, ESI†) and overpotentials (Fig. 3(c)). It was observed that NM modification significantly enhanced the catalytic activity of several TM–NM–GY catalysts. Particularly, Ag–v–GY and Ni–B–GY exhibited outstanding catalytic activity, with ultra-low overpotentials of 0.15 V and 0.08 V, approaching the theoretical limit. Additionally, a linear relationship resembling a volcano plot was observed between ΔG_{OOH} and η of TM–NM–GY, as shown in Fig. 3(d). The positions of Ag–v–GY and Ni–B–GY are quite near the peak of the volcano plot, further validating their superior catalytic activity for H_2O_2. This improvement is attributed to the alteration of the local coordination structure through B doping and C vacancy, resulting in ΔG_{OOH} values of Ni–B–GY (4.30 eV) and Ag–v–GY (4.07 eV), bringing them closer to the optimal catalyst with ΔG_{OOH} value of 4.22 eV.

3.3 Selectivity of TM–NM–GY (H_2O_2 *vs.* H_2O)

In addition to catalytic activity, selectivity also plays a crucial role in determining catalytic performance. The ORR can proceed through either a $2e^-$ pathway resulting in the production of H_2O_2 or a $4e^-$ pathway leading to the formation of H_2O, as shown in Fig. 4(a). The $4e^-$ pathway competes and suppresses the production of H_2O_2. Therefore, it is essential to evaluate the selectivity towards H_2O_2 and H_2O on TM–NM–GY based on their overpotentials ($\eta^{H_2O_2}$ and η^{H_2O}) as previously reported in the literature.[40] The Gibbs free energy diagrams for the $2e^-$ and $4e^-$ ORR pathways of all 20 types TM–NM–GY at zero potential and equilibrium potential are shown in Fig. S10 and S11 (ESI†). Furthermore, the corresponding $\eta^{H_2O_2}$ and η^{H_2O} values are summarized in Fig. 4(b) and Fig. S12 (ESI†). It is observed that all TM–NM–GY exhibit lower $\eta^{H_2O_2}$ values compared to η^{H_2O} except for Ag–GY, Pd–N–GY and Pd–B–GY, indicating their excellent selectivity towards H_2O_2 production. The introduction of B doping, N doping, and C vacancy in TM–GY results in a decrease in their overpotentials. Catalysts located above the dashed line in Fig. 4(b) demonstrate remarkable H_2O_2 selectivity, with darker colors indicating higher catalytic activity. Among these, Ni–B–GY demonstrates the lowest $\eta^{H_2O_2}$ (0.08 V) compared to η^{H_2O} (0.61 V).

A further analysis of selectivity was performed on Ag–v–GY and Ni–B–GY, which exhibited the highest catalytic activity. The $2e^-$ ORR at equilibrium potential (0.7 V) is shown in Fig. 4(c). On Ag–v–GY, the initial step (O_2 → OOH*) is spontaneous, while the PDS occurs at the final step (OOH* → H_2O_2) with a $\eta^{H_2O_2}$ of 0.15 V. Conversely, on Ni–B–GY, the final step is spontaneous and the PDS occurs at the initial step with a $\eta^{H_2O_2}$ of 0.08 V. The $4e^-$ ORR at the equilibrium potential (1.23 V) is shown in Fig. 4(d). For Ag–v–GY, only the third step (OOH* → O* + H_2O) is spontaneous, while the other steps are endothermic. The PDS occurs at the initial step (O_2 → OOH*) with an η^{H_2O} value of 0.38 V. For Ni–B–GY, only the initial step (O_2 → OOH*) is endothermic, while the remaining steps

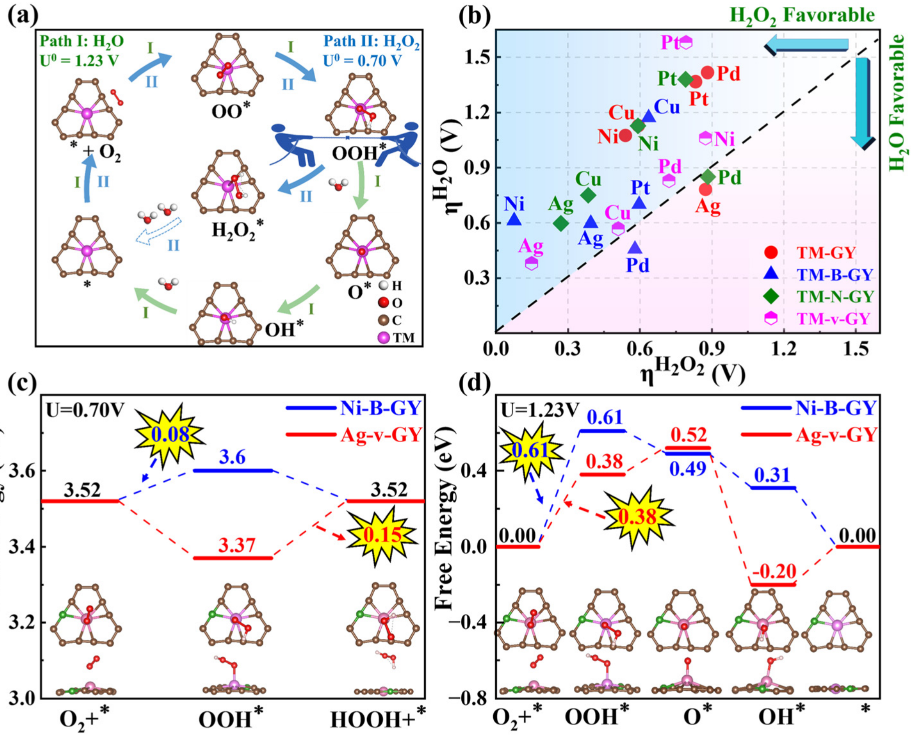

Fig. 4 The selectivity of TM–NM–GY catalysts: (a) Schematic illustration of the 2e$^-$ and 4e$^-$ ORR pathways. (b) Overpotential for 2e$^-$ and 4e$^-$ ORR. (c) and (d) Free energy diagrams comparing 2e$^-$ and 4e$^-$ ORR for Ag–v–GY and Ni–B–GY, highlighting their superior catalytic activity.

proceed spontaneously. Consequently, the PDS of Ni–B–GY (η^{H_2O} is 0.61 V) is the same as that of Ag–v–GY. The $\eta^{H_2O_2}$ values on Ag–v–GY and Ni–B–GY (0.15 and 0.08 V) are less than half of η^{H_2O} on them (0.38 and 0.61 V), indicating excellent selectivity.

3.4 Stability of TM–NM–GY

In addition to activity and selectivity, stability is another crucial factor for H_2O_2 electrocatalysts. The binding energy (E_{bind}) was used to preliminarily evaluate the structural stability of TM–NM–GY (TM = Ag, Cu, Ni, Pd, and Pt), as shown in

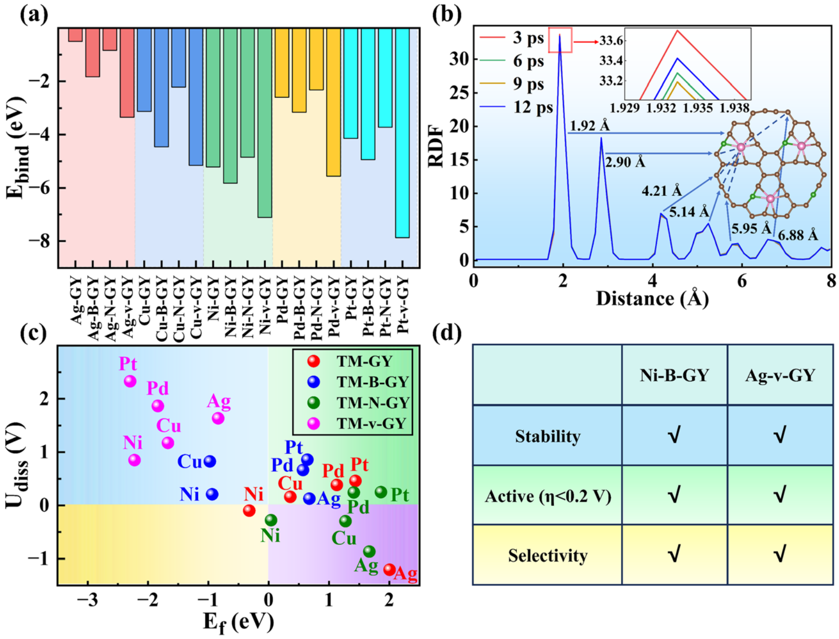

	Ni-B-GY	Ag-v-GY
Stability	√	√
Active (η<0.2 V)	√	√
Selectivity	√	√

Fig. 5 The stability of TM–NM–GY catalysts: (a) Binding energy (E_{bind}). (b) The RDF between the Ni and C for Ni–B–GY at 300 K and the configuration at 12 ps. (c) Dissolution potentials (U_{diss}) and formation energies (E_f). (d) The performances of Ni–B–GY and Ag–v–GY.

Fig. 5(a). Sixteen types of TM–NM–GY (TM = Cu, Ni, Pd, and Pt) exhibited negative binding energies less than −2 eV, indicating relatively good stability. Furthermore, both B doping and C vacancy significantly enhance the stability of TM–GY, with C vacancy showing the most substantial stability improvement effect. The strongest E_{bind} value of −7.87 eV was observed in Pt–v–GY.

The formation energy (E_f) is used to further evaluate thermodynamic stability:

$$E_f = E_{\mathrm{TM-NM-GY}} - E_{\mathrm{NM-GY}} - E_{\mathrm{TM}} \quad (9)$$

where $E_{\mathrm{TM-NM-GY}}$ and $E_{\mathrm{NM-GY}}$ refer to the energy of substrates with and without TM bonding, respectively, while E_{TM} is the energy of a single TM atom in its bulk. $E_f < 0$ eV were considered thermodynamically stable.[63] Therefore, Ni–, Ni–B–, Cu–B–, Ni–v–, Cu–v–, Ag–v–, Pt–v– and Pd–v–GY all thermodynamically stable, as shown in Fig. 5(c).

Furthermore, *ab initio* molecular dynamics simulations were conducted at 300 K for 12 ps to evaluate their thermodynamic stability (Fig. S13, ESI†). While Ag–GY and Ag–N–GY exhibited energy fluctuations suggesting limited stability, other TM–NM–GY catalysts showed minimal fluctuations and geometrical distortion, with TM atoms securely anchored within the GY cavity, indicating robust thermodynamic stability. Ni–B–GY was specifically studied due to its outstanding H_2O_2 catalytic activity (η = 0.08 V) and selectivity ($\eta^{H_2O_2}$ of 0.08 *vs.* η^{H_2O} of 0.61 V). The radial distribution function (RDF) in Fig. 5(b) analyzed the Ni–C interactions, revealing multiple peaks corresponding to Ni–C spacing, with a higher peak indicating a stronger interaction.[64,65] The consistent RDF patterns at different time points (3 ps, 6 ps, 9 ps, and 12 ps) suggest that the Ni–C bond remains stable throughout the kinetic process, further confirming its excellent thermodynamic stability.

After assessing the thermodynamic stability, the electrochemical stability was further examined through the dissolution potential U_{diss}[40,63] as follows:

$$U_{\mathrm{diss}} = U^0_{\mathrm{diss}} - (E_f)/ne \quad (10)$$

where U^0_{diss} represents the standard dissolution potential of the TM bulk and n is the number of electrons involved in the dissolution process. Electrochemical stability is determined by $U_{\mathrm{diss}} > 0$ V.[40,63] Fig. 5(c) illustrates that Ni–, Ag–, Ni–N–, Ag–N– and Cu–N–GY will dissolve in electrochemical environments due to their positive $U_{\mathrm{diss}} < 0$ V. Conversely, other TM–NM–GY with $U_{\mathrm{diss}} > 0$ V exhibit electrochemical stability. Additionally, B doping and C vacancy notably improve the electrochemical stability of the catalysts, validating the effectiveness of our modification approach. Ni–B–GY and Ag–v–GY, which exhibit

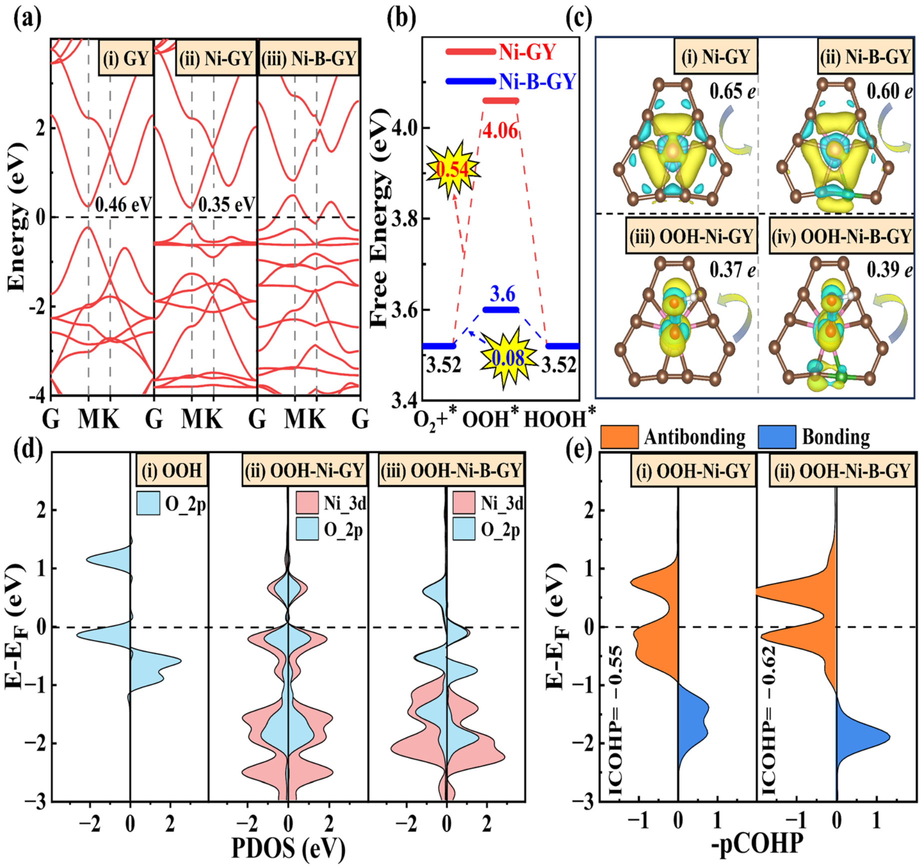

Fig. 6 (a) The band structure of GY, Ni–GY and Ni–B–GY. (b) Free energy diagrams comparing 2e⁻ ORR for Ni–GY and Ni–B–GY. (c) Charge density differences with and without OOH adsorbed on Ni–GY and Ni–B–GY. (d) The PDOS for OOH, OOH-Ni–GY and OOH-Ni–B–GY. (f) The COHP between the O (in OOH) and Ni for Ni–GY and Ni–B–GY.

the best catalytic activity, have positive U_{diss} values, indicating their exceptional electrochemical stability.

By conducting a comprehensive evaluation of the stability for the TM–NM–GY using thermodynamics, molecular dynamics, and electrochemical analyses, we confirmed that Ni–B–, Cu–B–, Ni–v–, Cu–v–, Ag–v–, Pt–v– and Pd–v–GY exhibit good stability, as shown in Fig. S14 (ESI†). Subsequently, after a comprehensive evaluation of activity, selectivity, and stability, we identified Ni–B–GY, Cu–v–GY and Ag–v–GY with excellent comprehensive catalytic performance, as shown in Fig. S15 (ESI†). Notably, Ni–B–GY and Ag–v–GY demonstrated exceptional catalytic performance with remarkably low overpotentials of 0.08 and 0.15 V (Fig. 5(d)).

3.5 Origin of high activity for H_2O_2 production on Ni–B–GY

Having confirmed the activity, selectivity, and stability of TM–NM–GY, we moved on to explore the origin of its activity. To achieve a deeper comprehension, we chose the Ni–B–GY with the best catalytic activity for analysis. The pristine GY material is a semiconductor with a bandgap of 0.46 eV (see Fig. 6(a)). Upon the introduction of Ni atoms, the band gap decreases to 0.35 eV for Ni–GY. Further introduction of B atoms causes the valence band maximum to shift upwards and cross the Fermi level (E_{F}), resulting in Ni–B–GY showing metallic properties. This combined introduction of TM and B significantly boosts the electrical conductivity, which is beneficial for electrocatalysis. At an equilibrium potential of 0.7 V, both Ni–B–GY and Ni–GY exhibit PDS in the first step, as shown in Fig. 6(b). The introduction of B atoms significantly enhances ΔG_{OOH}, which is the key reason for the improved catalytic activity.

Then, we explored the reasons behind the enhanced OOH* adsorption due to B doping. Moreover, charge transfer plays a crucial role in electrocatalysis. The charge density difference in Fig. 6(c) suggests that –C≡C– structure offers a greater number of empty orbitals compared to the –C═C– structure, which primarily facilitates charge transfer. During the reaction process, –C═C– acts as an electron donor, while –C≡C– not only serves as an anchor site for active TM, but also shoulders the roles of electron donation and transfer (Fig. S16, ESI†). The introduction of B leads to a charge transfer from Ni to OOH of 0.39 *e* for Ni–B–GY, surpassing the 0.37 *e* for Ni–GY. This increased charge transfer enhances the adsorption strength of OOH, thereby facilitating H_2O_2 production. The higher charge transfer is attributed to the lower electronegativity of B (2.04) compared to C (2.55). These differences in atoms disrupt the original charge balance and coordination structure symmetry, leading to the transformation from Ni–6C to Ni–B–5C and the formation of a C–B bond by breaking the conjugated C–C or C═C bonds. Consequently, the local coordination of B atoms effectively reduces the positive charge density of Ni-d-orbit-related electronic structures in Ni–B–GY. This results in a higher charge transfer from Ni to OOH, strengthening the adsorption strength of OOH and ultimately enhancing activity and selectivity for H_2O_2.

The projected density of states (PDOS) was used to elucidate the interaction between O 2p orbitals in OOH and Ni 3d orbitals, as shown in Fig. 6(d). The introduction of B atoms alters the symmetry of the coordination environment and charge density (Fig. S18, ESI†), leading to a stronger hybridization effect between Ni $d_{x^2-y^2}$ and O p_z orbitals near −1.8 eV below the Fermi level (E_{F}), as shown in Fig. S19 (ESI†). This results in an increased charge transfer from the 2π* and 3σ molecular orbitals of OOH to the unoccupied d orbitals of Ni, as shown in Fig. 6(c) and the donation and back-donation model in Fig. S17 (ESI†). The enhanced donation effect creates a lower bonding state, facilitating the adsorption of OOH. Furthermore, the introduction of B will boost the number of back-donated electrons from the partially occupied Ni 3d orbitals to the OOH 2π* molecular orbitals. Consequently, this conversion transforms some initially empty orbitals into occupied ones, favoring the formation of partially occupied orbitals in an antibonding state.

To further validate the interaction between Ni and O (Ni–O), we employed the COHP method to assess the Ni–O bonding strength of with and without B doping. This assessment considers both bonding states (blue region) and antibonding states (red region), as shown in Fig. 6(e). Our findings indicate that following B doping, the bonding state shifts downward, occupying lower energy levels, while the occupancy of bonded states above the E_{F} increases. The combined effects of bonding and antibonding states indicate that B doping enhances the OOH adsorption strength, thereby facilitating charge transfer during the catalytic reaction process and ultimately improving catalytic activity. Similar alterations in adsorption strength, charge transfer, and bonding state properties are also evident in OO* (see Fig. S20, ESI†). Ultimately, B doping not only enhances the d-2π* coupling facilitating the adsorption and activation of O_2 in preparation for subsequent H_2O_2 reactions,[4] but also contributes to the formation of lower bonding states for Ni–O, strengthening the adsorption of OO and OOH. The integrated COHP (ICOHP) was employed to quantitatively assess the Ni–O bonding interactions in OOH, with a lower value indicating stronger bond interactions.[4,66] After B doping, the ICOHP for Ni–O decreases from −0.55 to −0.62, indicating an enhancement in the Ni–O interaction, leading to a stronger adsorption of OOH and ultimately enhancing the catalytic activity.

4. Conclusions

In summary, this study presented a full picture (activity trends, electronic origins, and design strategies) for effectively screening and designing potential $2e^-$ ORR electrocatalysts for H_2O_2 production using TM–GY and TM–NM–GY SACs through a general four-step strategy. Initially, Ag–, Cu–, Ni–, Pd–, and Pt–GY were identified as promising SACs for H_2O_2 production out of 30 types of TM–GY. Subsequently, two reliable intrinsic activity descriptors φ_1 and φ_2 were established for screening and designing $2e^-$ ORR catalysts. Based on these descriptors, B doping and creating C vacancies were found to be effective strategies for further enhancing catalytic activity. Particularly, Ag–v–GY and Ni–B–GY demonstrated remarkable activity, selectivity, and stability with extremely low overpotentials of 0.15 V and 0.08 V, respectively. The analysis of the activity mechanism for Ni–B–GY revealed that the remarkable catalytic performance can be attributed to the doping of B atoms, which alters the coordination environment, enhances conductivity, facilitates electron transfer, and strengthens the hybridization between TM 3d and O 2p orbitals, leading to improved adsorption strength of OOH and enhanced catalytic performance. These findings are expected to inspire further exploration and design of high-performance SACs.

Data availability

The data supporting this article have been included as part of the ESI.†

Conflicts of interest

The authors declare that they have no known competing financial interests or personal relationships that could have appeared to influence the work reported in this paper.

Acknowledgements

This work was financially supported by the National Natural Science Foundation of China (12074048 and 12347101), the China Postdoctoral Science Foundation (2023M732903 and 2023T160537), the Sichuan Science and Technology Program (2024NSFSC1382) and the Chengdu Municipal Science and Technology Program (2022-YF05-00886-SN). The numerical calculations in this paper have been carried out in the Hefei advanced computing center.

References

1 M. Hu, W. Wu and H. Jiang, *ChemSusChem*, 2019, **12**, 2911–2935.
2 X. Shi, S. Siahrostami, G. L. Li, Y. Zhang, P. Chakthranont, F. Studt, T. F. Jaramillo, X. Zheng and J. K. Nørskov, *Nat. Commun.*, 2017, **8**, 701.
3 Y. Xia, X. Zhao, C. Xia, Z. Y. Wu, P. Zhu, J. Y. T. Kim, X. Bai, G. Gao, Y. Hu, J. Zhong, Y. Liu and H. Wang, *Nat. Commun.*, 2021, **12**, 4225.
4 W. Zhang, F.-L. Sun, Q.-J. Fang, Y.-F. Yu, J.-K. Pan, J.-G. Wang and G.-L. Zhuang, *J. Phys. Chem. C*, 2022, **126**, 2349–2364.
5 C. Zhang, W. Shen, K. Guo, M. Xiong, J. Zhang and X. Lu, *J. Am. Chem. Soc.*, 2023, **145**, 11589–11598.
6 Q. Chang, P. Zhang, A. H. B. Mostaghimi, X. Zhao, S. R. Denny, J. H. Lee, H. Gao, Y. Zhang, H. L. Xin, S. Siahrostami, J. G. Chen and Z. Chen, *Nat. Commun.*, 2020, **11**, 2178.
7 D. Iglesias, A. Giuliani, M. Melchionna, S. Marchesan, A. Criado, L. Nasi, M. Bevilacqua, C. Tavagnacco, F. Vizza, M. Prato and P. Fornasiero, *Chem.*, 2018, **4**, 106–123.
8 J. S. Jirkovský, I. Panas, E. Ahlberg, M. Halasa, S. Romani and D. J. Schiffrin, *J. Am. Chem. Soc.*, 2011, **133**, 19432–19441.
9 X. Sheng, N. Daems, B. Geboes, M. Kurttepeli, S. Bals, T. Breugelmans, A. Hubin, I. F. J. Vankelecom and P. P. Pescarmona, *Appl. Catal., B*, 2015, **176–177**, 212–224.
10 E. Pizzutilo, O. Kasian, C. H. Choi, S. Cherevko, G. J. Hutchings, K. J. J. Mayrhofer and S. J. Freakley, *Chem. Phys. Lett.*, 2017, **683**, 436–442.
11 A. Wang, J. Li and T. Zhang, *Nat. Rev. Chem.*, 2018, **2**, 65–81.
12 J. Liu, *ACS Catal.*, 2016, **7**, 34–59.
13 Z. Xue, M. Yan, X. Wang, Z. Wang, Y. Zhang, Y. Li, W. Xu, Y. Tong, X. Han, C. Xiong, W. Wang, M. Chen, B. Ye, X. Hong, L. Song, H. Zhang, L. M. Yang and Y. Wu, *Small*, 2021, **17**, 2101008.
14 Q. Yao, S.-Y. Lv, Z. Yu, Y.-C. Chang, C.-W. Pao, Z. Hu, L.-M. Yang, X. Huang, Q. Shao and J. Lu, *ACS Catal.*, 2023, **13**, 11023–11032.
15 S.-L. Li, Q. Li, Y. Chen, Y. Zhao and L.-Y. Gan, *Appl. Surf. Sci.*, 2022, **605**, 154828.
16 F. Li, H. Shu, C. Hu, Z. Shi, X. Liu, P. Liang and X. Chen, *ACS Appl. Mater. Interfaces*, 2015, **7**, 27405–27413.
17 Z. Yu, Y. Chen, J. Xia, Q. Yao, Z. Hu, W.-H. Huang, C.-W. Pao, W. Hu, X.-M. Meng, L.-M. Yang and X. Huang, *Nano Lett.*, 2024, **24**, 1205.
18 J. Yang, Z. Wang, C. X. Huang, Y. Zhang, Q. Zhang, C. Chen, J. Du, X. Zhou, Y. Zhang, H. Zhou, L. Wang, X. Zheng, L. Gu, L. M. Yang and Y. Wu, *Angew. Chem., Int. Ed.*, 2021, **60**, 22722–22728.
19 M. Zhu, C. Zhao, X. Liu, X. Wang, F. Zhou, J. Wang, Y. Hu, Y. Zhao, T. Yao, L.-M. Yang and Y. Wu, *ACS Catal.*, 2021, **11**, 3923–3929.
20 Z. Yang, X. Wang, M. Zhu, X. Leng, W. Chen, W. Wang, Q. Xu, L.-M. Yang and Y. Wu, *Nano Res.*, 2021, **14**, 4512–4519.
21 Z. Yu, S. Lv, Q. Yao, N. Fang, Y. Xu, Q. Shao, C. W. Pao, J. F. Lee, G. Li, L. M. Yang and X. Huang, *Adv. Mater.*, 2022, **35**, 2208101.
22 T. Gao, S. Yu, Y. Chen, X. Li, X. Tang, S. Wu, B. He, H. Lan, S. Li, Q. Yue and D. Xiao, *J. Colloid Interface Sci.*, 2023, **642**, 120–128.
23 S. Zhou, N. Liu, Z. Wang and J. Zhao, *ACS Appl. Mater. Interfaces*, 2017, **9**, 22578–22587.
24 T. Liu, X. Qu, Y. Zhang, X. Wang, Q. Dang, X. Li, B. Wang, S. Tang, Y. Luo and J. Jiang, *Chem. Eng. J.*, 2023, **457**, 141187.
25 S. Liu and J.-y Liu, *J. Power Sources*, 2022, **535**, 231449.
26 M.-R. Zhao, B. Song and L.-M. Yang, *ACS Appl. Mater. Interfaces*, 2021, **13**, 26109–26122.
27 D. Deng and L.-M. Yang, *ACS Appl. Mater. Interfaces*, 2023, **15**, 22012–22024.
28 X. Wang and L.-M. Yang, *Appl. Surf. Sci.*, 2022, **576**, 151839.
29 X. Wang and L.-M. Yang, *J. Mater. Chem. A*, 2022, **10**, 1481–1496.

30 X. Zhou, J. Shan, L. Chen, B. Y. Xia, T. Ling, J. Duan, Y. Jiao, Y. Zheng and S.-Z. Qiao, *J. Am. Chem. Soc.*, 2022, **144**, 2079–2084.

31 P. Wang, H. Yang, C. Tang, Y. Wu, Y. Zheng, T. Cheng, K. Davey, X. Huang and S.-Z. Qiao, *Nat. Commun.*, 2022, **13**, 3754.

32 S. Yadav, Z. Zhu and C. V. Singh, *Int. J. Hydrogen Energy*, 2014, **39**, 4981–4995.

33 S. L. Li, H. Yin, X. Kan, L. Y. Gan, U. Schwingenschlogl and Y. Zhao, *Phys. Chem. Chem. Phys.*, 2017, **19**, 30069–30077.

34 S. Ji, Z. Wang and J. Zhao, *J. Mater. Chem. A*, 2019, **7**, 2392–2399.

35 Z. He, Q. Liu, Y. Zhu, T. Tan, L. Cao, S. Zhao and Y. Chen, *ACS Appl. Energy Mater.*, 2020, **3**, 7039–7047.

36 X. Yao, Z.-W. Chen, Y.-R. Wang, X.-Y. Lang, Y.-F. Zhu, W. Gao and Q. Jiang, *Appl. Surf. Sci.*, 2020, **529**, 147183.

37 C. Wang, Y. Wang, Q. Guo, E. Dai and Z. Nie, *ACS Omega*, 2022, **7**, 21994–22002.

38 W. Ji, T.-X. Wang, X. Ding, S. Lei and B.-H. Han, *Coord. Chem. Rev.*, 2021, **439**, 213875.

39 Q. Li, Y. Li, Y. Chen, L. Wu, C. Yang and X. Cui, *Carbon*, 2018, **136**, 248–254.

40 X. Guo, S. Lin, J. Gu, S. Zhang, Z. Chen and S. Huang, *ACS Catal.*, 2019, **9**, 11042–11054.

41 X. Chen, X. Jiang and N. Yang, *Small*, 2022, **18**, 2201135.

42 C. Wang and C. Guo, *Int. J. Hydrogen Energy*, 2021, **46**, 33409–33419.

43 B. Li, S. Yu, M. Zhou, C. Chen, C. Lai, M. Zhang and H. Lin, *J. Mater. Chem. A*, 2022, **10**, 3905–3932.

44 W. Song, Z. Fu, P. Ma, X. Liu, Y. Guo, L. Fu and C. He, *Appl. Surf. Sci.*, 2023, **617**, 156550.

45 Y. Fu, D. Xu, Y. Wang, X. Li, Z. Chen, K. Li, Z. Li, L. Zheng and X. Zuo, *ACS Sustainable Chem. Eng.*, 2020, **8**, 8338–8347.

46 W. Zhang, Y. J. Gao, Q. J. Fang, J. K. Pan, X. C. Zhu, S. W. Deng, Z. H. Yao, G. L. Zhuang and J. G. Wang, *J. Colloid Interface Sci.*, 2021, **599**, 58–67.

47 G. Kresse and J. Furthmuller, *Phys. Rev. B: Condens. Matter Mater. Phys.*, 1996, **54**, 11169–11186.

48 G. Kresse and D. Joubert, *Phys. Rev. B: Condens. Matter Mater. Phys.*, 1999, **59**, 1758–1775.

49 J. P. Perdew, K. Burke and M. Ernzerhof, *Phys. Rev. Lett.*, 1996, **77**, 3865–3868.

50 T. Bučko, J. Hafner, S. Lebègue and J. G. Ángyán, *J. Phys. Chem. A*, 2010, **114**, 11814–11824.

51 S. Maintz, V. L. Deringer, A. L. Tchougréeff and R. Dronskowski, *J. Comput. Chem.*, 2013, **34**, 2557–2567.

52 S. Maintz, V. L. Deringer, A. L. Tchougréeff and R. Dronskowski, *J. Comput. Chem.*, 2016, **37**, 1030–1035.

53 A. Kulkarni, S. Siahrostami, A. Patel and J. K. Nørskov, *Chem. Rev.*, 2018, **118**, 2302–2312.

54 J.-S. Kim, J.-S. Kug and S.-J. Jeong, *Nat. Commun.*, 2017, **8**, 1674.

55 J. K. Nørskov, J. Rossmeisl, A. Logadottir, L. Lindqvist, J. R. Kitchin, T. Bligaard and H. Jónsson, *J. Phys. Chem. B*, 2004, **108**, 17886–17892.

56 A. J. Medford, A. Vojvodic, J. S. Hummelshøj, J. Voss, F. Abild-Pedersen, F. Studt, T. Bligaard, A. Nilsson and J. K. Nørskov, *J. Catal.*, 2015, **328**, 36–42.

57 H. Xu, D. Cheng, D. Cao and X. C. Zeng, *Nat. Catal.*, 2024, **7**, 207–218.

58 C. Ren, S. Lu, Y. Wu, Y. Ouyang, Y. Zhang, Q. Li, C. Ling and J. Wang, *J. Am. Chem. Soc.*, 2022, **144**, 12874–12883.

59 Y. Zhang, D. Wang, G. Wei, B. Li, Z. Mao, S.-M. Xu, S. Tang, J. Jiang, Z. Li, X. Wang and X. Xu, *JACS Au*, 2024, **4**, 1509–1520.

60 H. W. Kim, H. Park, J. S. Roh, J. E. Shin, T. H. Lee, L. Zhang, Y. H. Cho, H. W. Yoon, V. J. Bukas, J. Guo, H. B. Park, T. H. Han and B. D. McCloskey, *Chem. Mater.*, 2019, **31**, 3967–3973.

61 D. Navadeepthy, A. Rebekah, C. Viswanathan and N. Ponpandian, *Mater. Res. Bull.*, 2017, **95**, 1–8.

62 E. Jung, H. Shin, B. H. Lee, V. Efremov, S. Lee, H. S. Lee, J. Kim, W. Hooch Antink, S. Park, K. S. Lee, S. P. Cho, J. S. Yoo, Y. E. Sung and T. Hyeon, *Nat. Mater.*, 2020, **19**, 436–442.

63 X. Guo, J. Gu, S. Lin, S. Zhang, Z. Chen and S. Huang, *J. Am. Chem. Soc.*, 2020, **142**, 5709–5721.

64 K.-y Chen, J. Xia, S.-q Wang, R.-j Wu, W.-l Min, J.-y Wei, D.-s Hou and S. Mu, *Cem. Concr. Res.*, 2024, **146**, 105375.

65 Z. Yang, J. He, W. H. Lai, J. Peng, X. H. Liu, X. X. He, X. F. Guo, L. Li, Y. Qiao, J. M. Ma, M. Wu and S. L. Chou, *Angew. Chem., Int. Ed.*, 2021, **133**, 27292–27300.

66 H. Niu, X. Wang, C. Shao, Y. Liu, Z. Zhang and Y. Guo, *J. Mater. Chem. A*, 2020, **8**, 6555–6563.